# Dynamic interference in the photoionization of He by coherent intense high-frequency laser pulses: Direct propagation of the two-electron wave packets on large spatial grids

Anton N. Artemyev, Anne D. Müller, David Hochstuhl, Lorenz S. Cederbaum, and Philipp V. Demekhin

Phys. Rev. A **93**, 043418 — Published 25 April 2016

DOI: 10.1103/PhysRevA.93.043418

# Dynamic interference in the photoionization of He by coherent intense high-frequency laser pulses: Direct propagation of the two-electron wave packets on large spatial grids

Anton N. Artemyev,[1] Anne D. Müller,[1] David Hochstuhl,[2] Lorenz S. Cederbaum,[3] and Philipp V. Demekhin[1,4,*]

[1] *Institut für Physik und CINSaT, Universität Kassel, Heinrich-Plett-Str. 40, 34132 Kassel, Germany*
[2] *Institut für Theoretische Physik und Astrophysik, Leibnizstraße 15, 24098 Kiel, Germany*
[3] *Theoretische Chemie, Physikalisch-Chemisches Institut, Universität Heidelberg, Im Neuenheimer Feld 229, 69120 Heidelberg, Germany*
[4] *Research Institute of Physics, Southern Federal University, Stachki av. 194, 344090 Rostov-on-Don, Russia*

(Dated: April 5, 2016)

The direct ionization of the helium atom by intense coherent high-frequency short laser pulses is investigated theoretically from first principles. To this end, we solve numerically the time-dependent Schrödinger equation for the two-electron wave packet and its interaction with the linearly-polarized pulse by the efficient time-dependent restricted-active-space configuration-interaction method (TD-RASCI). In particular, we consider photon energies which are nearly resonant for the $1s \rightarrow 2p$ excitation in the $He^+$ ion. Thereby, we investigate the dynamic interference of the photoelectrons of the same kinetic energy emitted at different times along the pulse in the two-electron system. In order to enable observation of the dynamic interference in the computed spectrum, the electron wave packets were propagated on large spatial grids over long times. The computed photoionization spectra of He exhibit pronounced interference patterns the complexity of which increases with the decrease of the photon energy detuning and with the increase of the pulse intensity. Our numerical results pave the way for experimental verification of the dynamic interference effect at presently available high-frequency laser pulse sources.

PACS numbers: 33.20.Xx, 41.60.Cr, 82.50.Kx

## I. INTRODUCTION

The possibility of interference in the time domain was first discussed in the multiphoton absorption regime by optical lasers pulses [1–6]. Intense optical pulses couple different discrete electronic states of a system and cause relative ac Stark energy shifts [7], which follow the time-envelope of the pulse. As a consequence, the temporally coherent pulses may lead to the interference owing to excitation of the time-separated transient resonances on the rising and falling fronts of the pulse. Such interference appears as distinct multiple-peak pattern in the spectrum of particles emitted via relaxation of the system, as has been theoretically predicted for the strong field autoionization [1, 2], resonant fluorescence [3, 4], and resonant multiphoton ionization [5, 6] spectra. Later on, oscillations in the *total* multiphoton ionization yield were measured as a function of laser intensity and explained by the interference of electrons emitted at different times [8, 9].

The presently available attosecond lasers [10], high-order harmonic generation sources [11, 12], and free electron lasers [13, 14] allow one to produce pulses with photon energies, which are by far above the ionization threshold of any matter. These unprecedentedly strong and short high-frequency pulses enable one to reinvestigate various fundamental light-matter interaction processes under extreme field conditions (see, e.g., Refs. [15–36] and references therein). Recently, dynamic interference was also reinvestigated in the high-frequency regime [37–43]. It was identified theoretically in the (i) photoionization and above-threshold ionization (ATI) spectra of model anions [37, 38]; (ii) direct photoionization spectra of atoms [39, 40]; (iii) resonant Auger decay spectra of atoms induced by free electron laser pulses [41–43]; and (iv) sequential multiphoton ionization of atoms by high-frequency pulses [43]. In all those works, theoretical consideration was restricted to a single active electron.

Exposed to strong pulses, an atom with several electrons can undergo several ionization steps creating differently charged ions and even bare nuclei [15–18]. Moreover, a many-electron system exhibits usually several open ionization channels, and different final ionic states can be produced in each of the photoionization step. In the present work we study how the dynamic interference effect, investigated previously in the one-active-electron approximation, modifies in systems with more electrons. In particular, we investigate here the photoionization of He under conditions amenable to current experiments. The paper is organized as follows. Sec. II describes the process under consideration and outlines present theoretical approach and computational details. Results of numerical calculations are discussed and analyzed in Sec. III. We conclude with a brief summary.

## II. THEORY

### A. The process

The process relevant to the present study is schemati-

*Electronic address: demekhin@physik.uni-kassel.de

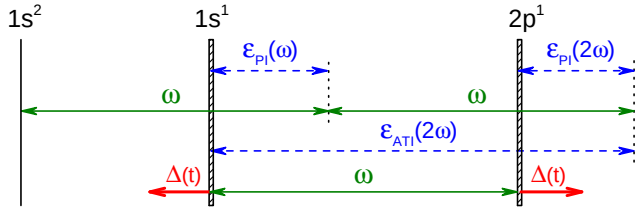


FIG. 1: (Color online) Sketch of the presently studied process, in which absorption of a photon of energy $\omega$ from a high-frequency pulse promotes one of the two electrons of He into the photoionization (PI) continuum of energy $\varepsilon_{\rm PI}$. Subsequent absorption of another nearly-resonant photon from the same pulse can either couple the $1s$ and $2p$ states of the second electron remaining in the $He^+$ ion, or promote the photoelectron into continuum state of higher energy $\varepsilon_{\rm ATI}$ via the above threshold ionization (ATI) process. The two coupled ionization thresholds $He^+(1s^1)$ and $He^+(2p^1)$ repel each other and follow a time-dependent energy shifts $\Delta(t)$ provided by the laser pulse. These shifts result in the dynamic interference in photoelectron spectrum of He.

cally drawn in Fig. 1. It implies a direct photoionization of the He atom by a coherent intense laser pulse with a carrier frequency close to the $He^+(1s \rightarrow 2p)$ excitation energy. The resonant photon energy $\omega = 1.50$ a.u. $=$ 40.817 eV is larger than the ionization potential of neutral He (24.587 eV [44]), but smaller than the ionization potential of $He^+$ (54.418 eV [44]). The intense resonant laser pulse couples the $He^+(1s^1)$ electronic state, remaining after photoionization, with the $He^+(2p^1)$ state, and creates a Rabi doublet by the ac Stark [7] or Autler-Townes [45] effect. The energy splitting between these ionic states adiabatically increases and decreases, respectively, when the pulse arrives and expires [43]. Consequently, the energy of photoelectrons, which see these ionic states as their photoionization thresholds, follows the pulse intensity envelope too. This gives rise to dynamic interference of photoelectrons emitted with the same kinetic energy on the rising and falling edges of the pulse [39].

We should note that the described process was originally proposed in our previous work [39]. In the supplemental material document of this reference, it was considered as the two-step process, in which the dynamics of the photoelectron was treated separately from that of the electron remaining in the ion. The latter introduces the time-dependent energy shift to the ionization threshold included in the former. In the present work, we consider the aforementioned coupled dynamics of the two electrons of He simultaneously. We should also notice that the processes with similar conditions, i.e., where the carrier frequency of the driving pulse was chosen to be resonant for the transitions between the final states of atomic Auger decay [19], as well as atomic [21] and molecular [26] photoionization, were already discussed in the literature. However, dynamic interference was neglected in those theoretical treatments or considered to be irrelevant for those processes owing to the laser field conditions.

Theoretical description of the presently studied process requires the solution of the time-dependent Schrödinger equation for the two-electron wave function $\Psi(\vec{r}_1, \vec{r}_2, t)$ of He exposed to intense coherent linearly-polarized laser pulse. In the electric dipole approximation, the total Hamiltonian of the system reads (atomic units are used throughout)

$$\hat{H}(t) = -\frac{1}{2}\vec{\nabla}_1^2 - \frac{1}{2}\vec{\nabla}_2^2 - \frac{2}{r_1} - \frac{2}{r_2} + \frac{1}{|\vec{r}_1 - \vec{r}_2|} + (z_1 + z_2)\,\mathcal{E}_0\, g(t)\cos(\omega t). \quad (1)$$

Here, $g(t)$ is the time-envelope of the pulse, $\omega$ is its carrier frequency, and $\mathcal{E}_0$ is the peak amplitude related with the peak intensity via $I_0 = \frac{1}{8\pi\alpha}\mathcal{E}_0^2$, where $\alpha \simeq 1/137.036$ is the fine structure constant, and 1 a.u. of intensity is equal to $6.43641\times10^{15}$ W/cm$^2$.

Desirable theoretical and computational approaches for atoms, required to propagate multi-electron wave packets in real time and space, are already available [46–58]. A straightforward implementation of the most accurate multi-configuration time-dependent Hartree-Fock (MCTDHF) method [46–51] to the solution of the present problem is a formidable computational task, even if it assumes propagation of only two active electrons in He. As has been demonstrated in our previous work [59], in order to allow the dynamic interference to occur, one has to propagate the undisturbed photoelectron wave packet during the pulse, without implying a complex absorption potential at the boundary. This requires radial spatial grids of at least $10^4$ a.u., even for relatively short few femtosecond ionizing pulses.

In order to tackle this challenging computational problem, we restricted the present theoretical consideration only to the dominant relevant physical processes evoked by the high-frequency pulse in He (see Fig. 1 and its description in the text). In particular, we neglected the very weak two-photon non-sequential double-ionization of He, which may occur already at the photon energies above $\omega = 39.508$ eV [51]. In addition, we forbad the second electron in the $He^+$ ion to be ionized, since this requires a sequential absorption of at least three photons from the pulse, i.e., by the $He^+(1s \rightarrow 2p)$ excitation and subsequent ionization. We thus keep one of the electrons always bound to the nucleus. Finally, we limited the two-electron space of active configurations as justified in Sec. II C. Hence, the time-dependent restricted-active-space configuration-interaction method (TD-RASCI, [52, 57, 58]), which can also be viewed as a restricted form of MCTDHF, was the computational approach of our choice. It is known to allow for a considerable simplification of the problem by a clever selection of the active configurational space.

### B. Theoretical approach

The present theoretical approach is based on the par-

ticular realization of the TD-RASCI method described in Ref. [52]. The implemented numerical procedure is partly reported in our previous works Refs. [59, 60]. Therefore, only its essential relevant points are outlined below. Briefly, the radial coordinate is described by the finite-element discrete-variable representation (FEDVR) basis set of the normalized Lagrange polynomials $\chi_{ik}(r)$, constructed over a Gauss-Lobatto grid $\{r_{ik}\}$ as introduced in Ref. [61–63]:

$$\chi_{ik}(r) = \frac{1}{\sqrt{w_{ik}}} \prod_{\mu \neq k} \frac{r - r_{i\mu}}{r_{ik} - r_{i\mu}}. \tag{2}$$

Here, index $i$ runs over the finite intervals $[r_i, r_{i+1}]$ and index $k$ counts the basis functions in each interval. As in [60], we further introduce the basis element in the three-dimensional space:

$$\xi_\lambda(\vec{r}) \equiv \xi_{ik,\ell m}(\vec{r}) = \frac{\chi_{ik}(r)}{r} Y_{\ell m}(\theta, \varphi). \tag{3}$$

As justified in the preceding section, we use two different one-electron spatial basis sets for the two electrons in He. In particular, dynamics of the electron which remains bound to the nucleus is described by a few selected localized orbitals $\{\phi_{n\ell m}(\vec{r}) \equiv \phi_\alpha(\vec{r})\}$. These stationary orbitals are composed of the basis elements $\xi_\lambda$ as

$$\phi_\alpha(\vec{r}) = \sum_\lambda d_\lambda^\alpha \, \xi_\lambda(\vec{r}), \tag{4}$$

and they are normalized according to the condition

$$\langle \phi_\alpha | \phi_{\alpha'} \rangle = \delta_{\alpha,\alpha'} = \delta_{n,n'} \delta_{\ell m, \ell' m'}. \tag{5}$$

In addition, we introduce the time-dependent wave packets of a photoelectron $\{\psi_{\ell m}^\alpha(\vec{r}, t) \equiv \psi_\beta(\vec{r}, t)\}$

$$\psi_\beta(\vec{r}, t) = \sum_\lambda c_\lambda^\beta(t) \, \xi_\lambda(\vec{r}), \tag{6}$$

which are constrained by the following condition

$$\langle \phi_\alpha | \psi_\beta(t) \rangle = 0, \quad \forall \; \alpha, \beta, t. \tag{7}$$

The wave-packets (6) are built to be orthogonal to all discrete orbitals $\phi_\alpha$. Therefore, the full dynamics of the photoelectron in the whole discrete and continuous spectrum can be described by the unification of the two one-electron basis sets $\{\phi_\alpha \cup \psi_\beta\}$.

Since the Hamiltonian (1) preserves the total spin of the $1s^2 \; {}^1S$ singlet ground state of He, the spatial part of the two-electron wave function must be symmetric with respect to permutation of two coordinates $\vec{r}_1$ and $\vec{r}_2$. We thus introduce the following symmetrized ansatz for the total two-electron wave function $\Psi(\vec{r}_1, \vec{r}_2, t)$

$$\begin{aligned}\Psi(\vec{r}_1, \vec{r}_2, t) &= \sum_\alpha a_\alpha(t) \phi_\alpha(\vec{r}_1) \phi_\alpha(\vec{r}_2) \\ &+ \sum_{\alpha > \alpha'} b_{\alpha\alpha'}(t) \frac{1}{\sqrt{2}} \left[ \phi_\alpha(\vec{r}_1) \phi_{\alpha'}(\vec{r}_2) + \phi_{\alpha'}(\vec{r}_1) \phi_\alpha(\vec{r}_2) \right] \\ &+ \sum_{\alpha\beta} \frac{1}{\sqrt{2}} \left[ \phi_\alpha(\vec{r}_1) \psi_\beta(\vec{r}_2, t) + \psi_\beta(\vec{r}_1, t) \phi_\alpha(\vec{r}_2) \right], \end{aligned} \tag{8}$$

where the one-electron basis is defined in Eqs. (4–7). The present calculations were performed by using the two-electron wave functions with well-defined total orbital angular momentum quantum numbers $L$ and $M$, which were constructed via usual Clebsch-Gordon expansion [64] over electronic states with given quantum numbers $\ell$ and $m$.

The matrix elements of the Hamiltonian (1) can be computed as described in detail in Refs. [59–63]. For completeness, we list here final working expressions in the basis of the three-dimensional elements (3). The matrix element of the one-electron kinetic energy operator reads (note that $\lambda \equiv \{ik, \ell m\}$ is four-dimensional index)

$$\begin{aligned}\langle \xi_\lambda | -\frac{1}{2} \vec{\nabla}^2 | \xi_{\lambda'} \rangle = \delta_{\ell m, \ell' m'} \Bigg\{ &\frac{\ell(\ell+1)}{2 r_{ik}^2} \, \delta_{ik,i'k'} \\ &+ \frac{1}{2} \left( \delta_{i,i'} + \delta_{i,i'\pm 1} \right) \int_0^\infty dr \frac{d}{dr} \chi_{ik}(r) \frac{d}{dr} \chi_{i'k'}(r) \Bigg\}. \end{aligned} \tag{9}$$

It can be analytically evaluated in terms of the first derivatives of the basis functions (2) as

$$\begin{aligned}\chi'_{ik}(r_{ik'}) &= \frac{(r_{ik} - r_{ik'})^{-1}}{\sqrt{w_{ik}}} \prod_{\mu \neq k, k'} \frac{r_{ik'} - r_{i\mu}}{r_{ik} - r_{i\mu}}, \quad k \neq k'; \\ &= \frac{1}{\sqrt{w_{ik}}} \sum_{\mu \neq k} (r_{ik} - r_{i\mu})^{-1}, \quad k = k'. \end{aligned} \tag{10}$$

The matrix element of the one-electron potential energy operator is given by:

$$\langle \xi_\lambda | -\frac{2}{r} | \xi_{\lambda'} \rangle = -\frac{2}{r_{ik}} \delta_{\ell m, \ell' m'} \delta_{ik, i'k'}. \tag{11}$$

The dipole transition matrix element for the interaction with the linearly-polarized field can be computed via:

$$\langle \xi_\lambda | z | \xi_{\lambda'} \rangle = r_{ik} \, \delta_{ik,i'k'} \sqrt{\frac{4\pi}{3}} \langle \ell m | 1 \, 0 | \ell' m' \rangle, \tag{12}$$

where $\langle \ell m | KQ | \ell' m' \rangle$ stands for the integral of the three spherical harmonics [65].

The matrix element of the two-electron Coulomb operator is evaluated using its standard expansion over spherical harmonics [64]

$$\begin{aligned}\left\langle \xi_\lambda \xi_{\lambda'} \left| \frac{1}{|\vec{r}_1 - \vec{r}_2|} \right| \xi_{\lambda''} \xi_{\lambda'''} \right\rangle = \\ \sum_{KQ} \frac{4\pi}{2K+1} \left\langle \chi_{ik} \chi_{i'k'} \left| \frac{r_<^K}{r_>^{K+1}} \right| \chi_{i''k''} \chi_{i'''k'''} \right\rangle \\ \times \langle \ell m | KQ | \ell'' m'' \rangle \langle \ell''' m''' | KQ | \ell' m' \rangle^*, \end{aligned} \tag{13}$$

where $r_<$ and $r_>$ are, respectively, the smallest and the largest of $r_1$ and $r_2$ values. The radial matrix element in Eq. (13) can be further evaluated as [63]

$$\begin{aligned}\left\langle \chi_{ik} \chi_{i'k'} \left| \frac{r_<^K}{r_>^{K+1}} \right| \chi_{i''k''} \chi_{i'''k'''} \right\rangle = \delta_{ik,i''k''} \delta_{i'k',i'''k'''} \\ \times \left( \frac{2K+1}{r_{i'k'} \sqrt{w_{i'k'}} \, r_{ik} \sqrt{w_{ik}}} \, [2T]^{-1}_{i'k',ik} + \frac{r_{i'k'}^K \, r_{ik}^K}{R_{max}^{2K+1}} \right), \end{aligned} \tag{14}$$

where $T_{ik,i'k'}$ is the matrix of the one-electron kinetic energy operator defined in braces of Eq. (9) with $\ell = K$, and $R_{max}$ is the last point of the radial grid.

In order to follow time-evolution of the total wave function (8), we collect the time-dependent expansion coefficients $a_\alpha(t)$, $b_{\alpha\alpha'}(t)$, and $c_\lambda^\beta(t)$ in a single vector $\vec{A}(t)$, which is propagated according to the Hamiltonian (1) with the matrix elements given by Eqs. (9–14):

$$\vec{A}(t) = \exp\left\{-iP\hat{H}(t)P\right\}\vec{A}(0). \qquad (15)$$

Here, the one-particle projector, $P = 1 - \sum_\alpha |\phi_\alpha\rangle\langle\phi_\alpha|$, acts on the $\left\{c_\lambda^\beta(t)\right\}$ part of the vector $\vec{A}(t)$ to ensure constrain (7). The propagation was managed by the short-iterative Lanczos method employing the algorithm of Ref. [66]. The multi-configurational initial ground state of the He atom in the absence of the field (i.e., the $\vec{A}(0)$ vector) was obtained via the imaginary time propagation. The three-dimensional momentum distribution of the emitted photoelectrons can be obtained from the Fourier transformation of the final electron wave packets at large times $\psi_\beta(\vec{r}) = \psi_\beta(\vec{r}, t = \infty)$. Because of the normalization condition (5), the total photoemission probability is given by

$$W(\vec{k}) = \frac{1}{(2\pi)^3}\sum_\beta \left| \int \psi_\beta(\vec{r})\, e^{-i\vec{k}\cdot\vec{r}} d^3\vec{r} \right|^2 . \qquad (16)$$

### C. Computational details

We, first, discuss the basis set of the discrete functions $\phi_\alpha$ taken for the bound electron in He and justify the present restrictions to the active space of configurations in Eq. (8). In order to be as close as possible to the ground state of neutral He, we include the $1s_{\rm HF}$ Hartree-Fock orbital in this basis set. Thereby, the two-electron ansatz (8) includes the $|1s_{\rm HF}^2\rangle$ configuration, as well as the corresponding $|1s_{\rm HF}\psi_{\ell m}^{1s}\rangle$ configurations. The former approximates the ground states of He, whereas the latter describes the one-photon – one-electron ionization in the $\psi_{\ell m}^{1s}$ continuum. Apart from the $1s_{\rm HF}$ orbital, the present one-electron basis set $\phi_\alpha$ includes the $2p_{ion}$ orbital of $He^+$. Thereby, the active space is extended to the $|2p_{ion}\psi_{\ell m}^{2p}\rangle$, and the $|1s_{\rm HF}2p_{ion}\rangle$ and $|2p_{ion}^2\rangle$ configurations. The former allows for the $1s_{\rm HF} \to 2p_{ion}$ excitation in the ion, which gives rise to the dynamic interference, whereas the latter two configurations ensure completeness of the present configurational space.

Although the already selected active space is sufficient to describe the dynamic interference effect, it yields low $1s_{\rm HF} \to 2p_{ion}$ excitation energy and underestimates the resonant carrier frequency. In order to correct for this inaccuracy, one should allow for relaxation of the $1s_{\rm HF}$ orbital in the ion to the $1s_{ion}$ orbital (the radial parts of the $1s_{\rm HF}$ and $1s_{ion}$ orbitals orbitals are compared in the upper panel of Fig. 2). For this purpose, the basis set $\phi_\alpha$

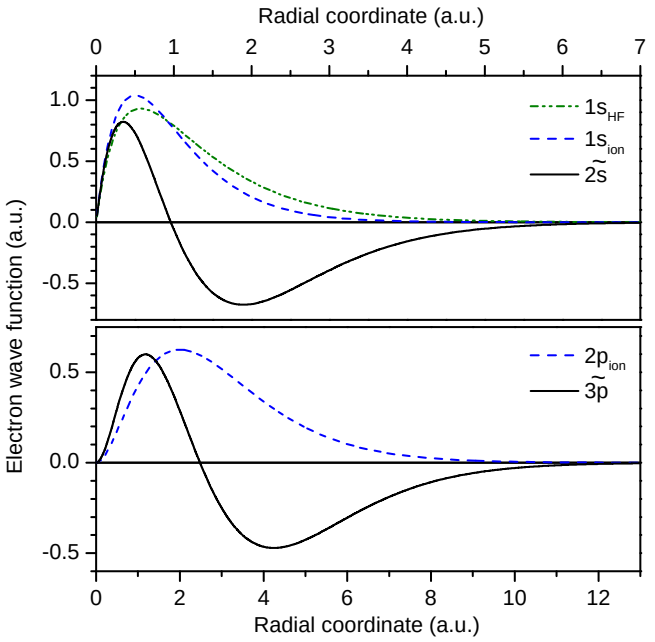


FIG. 2: (Color online) Radial parts of the one-electron functions, $r\cdot\phi_\alpha(r)$, used as the basis functions for the bound electron in the two-electron TD-RASCI ansatz Eq. (8). Shown are the $1s_{\rm HF}$ Hartree-Fock orbital of the He atom, $1s_{ion}$ and $2p_{ion}$ orbital of the $He^+$ ion, and the correlation functions $\widetilde{2s}$ and $\widetilde{3p}$ defined via Eqs. (17) and (19), respectively.

must include a complete set of the $ns_{ion}$ functions, which is rather complicated. However, there is an alternative procedure to describe the $1s_{\rm HF} \to 1s_{ion}$ relaxation in the ion by a single function.

Here, we included the following normalized difference between those two orbitals in the basis set $\phi_\alpha$

$$|\widetilde{2s}\,\rangle = N_{2s}\left(\,|1s_{ion}\rangle - |1s_{\rm HF}\rangle\langle 1s_{\rm HF}|1s_{ion}\rangle\,\right), \qquad (17)$$

where $N_{2s}$ stands for the normalization coefficient. The radial part of the $\widetilde{2s}$ function is depicted in the upper panel of Fig. 2 by solid line. This function satisfies the condition (5), i.e., it is orthogonal to the $1s_{\rm HF}$ orbital. It is also localized in the same region as the $1s_{\rm HF}$ and $1s_{ion}$ functions. Therefore, a proper mixture of the $1s_{\rm HF}$ and $\widetilde{2s}$ functions will yield the required $1s_{ion}$ orbital. In order to allow for this relaxation, we introduce the $|\widetilde{2s}\,\psi_{\ell m}^{2s}\rangle$ configuration in the active space. Including this configuration ensures correct value of the $1s_{ion} \to 2p_{ion}$ excitation energy of 1.50 a.u. Besides, configurations $|1s_{\rm HF}\widetilde{2s}\,\rangle$, $|\widetilde{2s}\,2p_{ion}\rangle$, and $|\widetilde{2s}^{\,2}\rangle$ need also to be included in the active space for completeness.

So far, the present active space allows for the most probable $1s_{ion} \to 2p_{ion}$ excitation in the ion. However, the quantum motion of the higher $np_{ion}$ states driven by the strong pulse may also influence dynamics of the whole process. This is especially important for the photon energies slightly above the resonant energy, where the next closest $3p_{ion}$ state is already involved. In order to allow

for such $1s_{ion} \to np_{ion}$ excitations in the ion, all those states need to be included in the basis set $\phi_\alpha$, which is rather expensive. Here, we imply the technique [67–69] and describe those transitions in an effective way by the single correlation function $\widetilde{3p}$. To this end, we construct and diagonalize the following matrix

$$\begin{pmatrix} E(1s_{ion})+\omega & \langle 1s_{ion}|\hat{z}|2p_{ion}\rangle & \dots & \langle 1s_{ion}|\hat{z}|np_{ion}\rangle & \dots \\ \langle 2p_{ion}|\hat{z}|1s_{ion}\rangle & E(2p_{ion}) & 0 & 0 & 0 \\ \dots & 0 & \dots & 0 & 0 \\ \langle np_{ion}|\hat{z}|1s_{ion}\rangle & 0 & 0 & E(np_{ion}) & 0 \\ \dots & 0 & 0 & 0 & \dots \end{pmatrix} \tag{18}$$

Here, $\langle n'\ell'_{ion}|\hat{z}|n\ell_{ion}\rangle$ are the corresponding dipole transition matrix elements in the ion.

The correlation function $\widetilde{3p}$ can now be computed with the help of the eigenvector $\left\{v_n^{1s}\right\}$ of matrix (18), which genealogically corresponds to the $1s_{ion}$ basis state

$$|\widetilde{3p}\rangle = N_{2p} \sum_{n>2} v_n^{1s} \, |np_{ion}\rangle. \tag{19}$$

Here, $N_{2p}$ stands for the normalization coefficient. This function is orthogonal to the $2p_{ion}$ function by its construction. The condition (5) is thus fulfilled. The radial parts of the $2p_{ion}$ and $\widetilde{3p}$ functions are compared in the lower panel of Fig. 2. One can see that the latter is localized around the former, and since $3p_{ion}$ function provides the major contribution to the sum (19), the $\widetilde{3p}$ function has one knot. The correlation function (19) effectively includes contributions from the whole $np_{ion}$ spectrum, apart from the explicitly included $2p_{ion}$ state. In order to allow for the $1s_{ion} \to \widetilde{3p}$ excitation to take place, we include the $|\widetilde{3p}\,\psi_{\ell m}^{3p}\rangle$ configuration, as well as the $|1s_{\rm HF}\widetilde{3p}\rangle$, $|\widetilde{2s}\,\widetilde{3p}\rangle$, $|2p_{ion}\widetilde{3p}\rangle$, and $|\widetilde{3p}^{\,2}\rangle$ configurations in the present active space.

The presently computed energy of the ground state of neutral He, obtained by the imaginary time propagation of the chosen active configurational space in the restricted radial interval of $r \le 50$ a.u., is equal to $E(1s^2) = -2.89384$ a.u. Since our active space allows for an exact numerical description of the $\mathrm{He}^+(1s^1)$ and $\mathrm{He}^+(2p^1)$ states, the theoretical ionization potential of He amounts to: $IP = E(1s^1) - E(1s^2) = -2.0 + 2.89384 = 0.89384$ a.u. $= 24.323$ eV. It is by $+0.873$ eV larger than the Hertree-Fock value of 23.450 eV, and only by $-0.264$ eV smaller than its experimental value of 24.587 eV [44]. In order to eliminate this difference between the theoretical and experimental ionization potentials, the photoelectron energy in all computed spectra was corrected by this value of $-0.264$ eV. As the consequence, photoelectron peaks in the computed spectra in Figs. 3–6 have correct energy positions, which facilitates comparison with possible experiments in the future.

As was suggested in the supplemental material document of our previous work Ref. [39], the present calculations were performed for a Gaussian-shaped pulse with the time-envelope $g(t) = e^{-t^2/\tau^2}$ and the pulse duration of $\tau = 30$ fs. The two-electron wave packets were propagated in the time-interval of $[-75$ fs$, +75$ fs$]$ centered around the pulse maximum. At the interval boundaries, the field amplitude falls by almost three orders of magnitude. For the photon energies used, the ATI electrons indicated in Fig. 1 have momenta of $k \sim 2.0$ a.u. During the propagation time of 150 fs $\approx 6200$ a.u. they may move off the nucleus by about $R_{max} \sim 12000$ a.u. In order to avoid hitting the outward grid boundary by the fast electrons during the whole propagation, this value of $R_{max}$ was chosen as the radial grid size. The interval $[0, R_{max}]$ was covered by 4800 equidistant finite elements of the 2.5 a.u. size, each represented by 10 Gauss-Lobatto points. In order to be able to describe ATI electrons, the wave packets $\psi_\beta$ with $\ell = 0, 1,$ and 2 were included in the present active space. The convergence of the solution with respect to the chosen computational parameters has been ensured.

A typical calculation discussed at the very beginning of the next section requires approximately 20 Gb memory and, in average, about 300 days for a single contemporary computer core. In order to be able to perform such time-consuming numerical calculations in a reasonable time, the propagation procedure was parallelized, and calculations were performed in the multiple-processor regime.

## III. RESULTS AND DISCUSSION

### A. Propagation of two-electron wave packet

An overview of the computational results obtained for the Gaussian-shaped pulse with the resonant carrier frequency of 1.50 a.u., peak intensity of $10^{14}$ W/cm$^2$, and duration of 30 fs is given in Fig. 3. The upper panel depicts the final radial wave packet density computed after the laser pulse has expired. In this wave packet, a clear hump with the maximum around $r = 4000$ a.u. represents the slow photoelectrons released by the photoionization (see below). The shoulder around $r = 8000$ a.u. describes faster electrons emitted via the ATI process. The electron energy spectrum obtained via Eq. (16) is depicted in the lower panel of Fig. 3. Assignments of the observed structures, made on the base of the main contribution to the spectrum, are also given in the figure near each peak.

The two groups of peaks are clearly visible in this computed energy distribution. The low-energy group corresponds to the photoionization process. In particular, the double-peak structure in the energy range of 16.0–16.5 eV corresponds to the Autler-Townes doublet of the $1s$ and $2p$ states of the $\mathrm{He}^+$ ion. It is produced by the one-photon ionization of the ground state and by the two-photon ionization and subsequent $1s \to 2p$ excitation in the ion. The low energy peaks at about $\varepsilon = 9.6$ and 5.2 eV correspond, respectively, to the population of the $\widetilde{2s}^{\,1}$ and $\widetilde{3p}^{\,1}$ states of $\mathrm{He}^+$ via the one- and two-photon

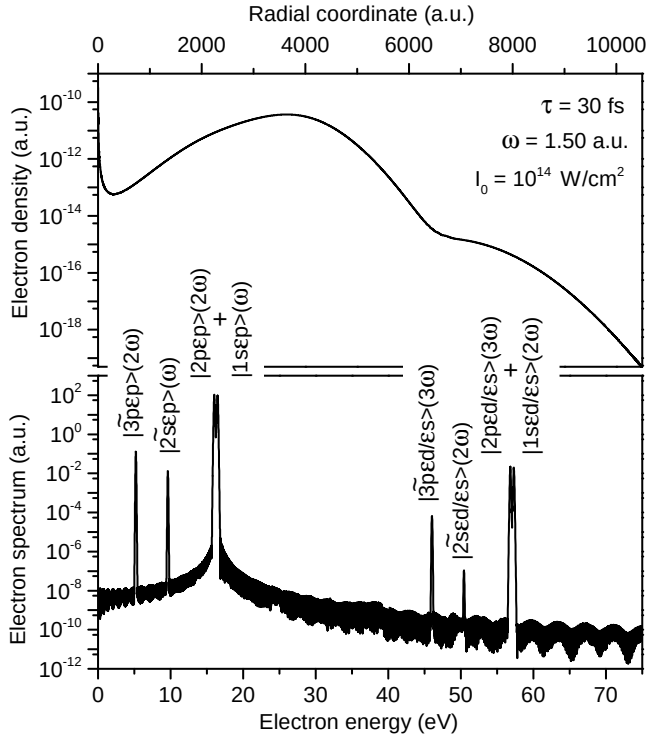


FIG. 3: The final photoelectron radial density (*upper panel*) and the final photoelectron spectrum (*lower panel*) after the intense linearly-polarized Gaussian-shaped pulse has expired. The pulse duration $\tau$, carrier frequency $\omega$, and peak intensity $I_0$, used in the calculations, as well as assignments of the main structures in the spectrum are indicated in the figure. Note the logarithmic scales on the vertical axes. Here and below, the electron energy was corrected by $-0.264$ eV for the difference between the theoretical and experimental ionization potentials (see Sec. II C for details).

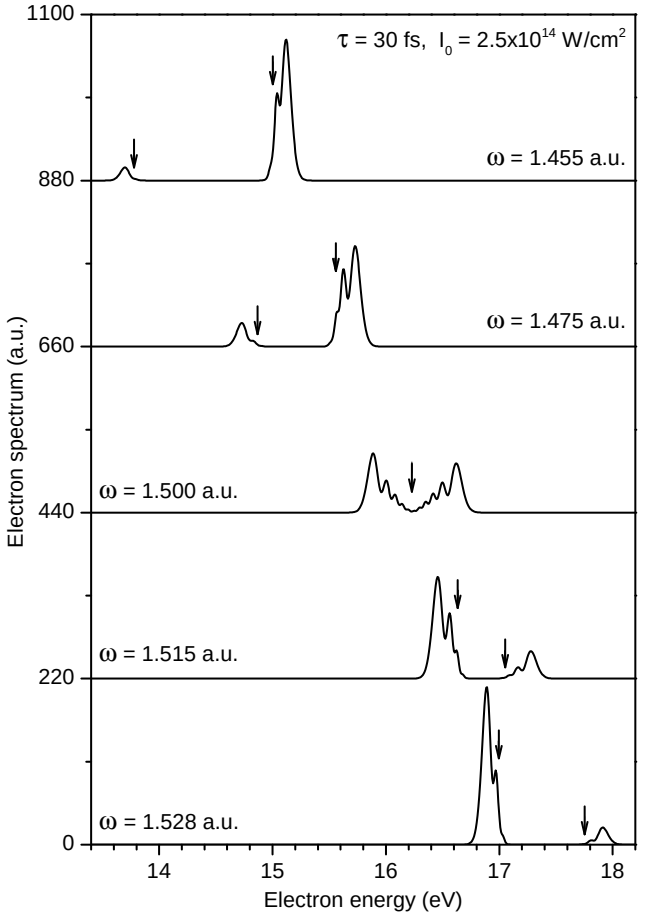


FIG. 4: Photoionization spectra of the helium atom computed for Gaussian-shaped pulses of 30 fs duration and peak intensity of $2.5 \times 10^{14}$ W/cm$^2$ for different carrier frequencies (indicated near each spectrum) around the $1s \rightarrow 2p$ resonant excitation in the $He^+$ ion. The photoelectron energies expected in the weak field regime are indicated by the vertical down-arrows. For the carrier frequencies below 1.5 a.u., the shift of the $1s$ threshold is negative, which results in the positive shift in the corresponding major part of the electron spectrum. On the contrary, the shift of the $2p$ threshold is positive, and for the associated minor part of the spectrum it is thus negative. For the frequencies above 1.50 a.u., the shift of the $1s$ threshold is positive and of the $2p$ threshold is negative, which results in the negative shift in the corresponding major part of the spectrum and in the positive shift in its minor part. The complexity of the dynamic interference patterns in the spectrum increases with the decrease of the photon energy detuning. The resonant carrier frequency of 1.50 a.u. produces nearly symmetric Autler-Townes doublet structured by distinct dynamic interference patterns.

absorption. These weak artificial structures are characteristic for the present choice of CI ansatz (Sec. II C). They comprise an integral contribution of all shake-up photoionization processes populating higher in energy realistic $ns^1$ and $np^1$ states of $He^+$, except the explicitly involved $He^+(1s^1)$ and $He^+(2p^1)$ thresholds. The high-energy group of peaks in the spectrum is separated from the low-energy group by the resonant photon energy of 40.817 eV. The former group corresponds one-by-one to the latter one, and it represents thereby the ATI processes involving absorption of an additional photon from the pulse. Due to the limitations of the present CI ansatz, these ATI structures were excluded from the analysis of the dynamic interference effect.

The presently computed photoionization spectra are collected in Figs. 4 and 5. In Fig. 4, the photon energy increases from top to bottom across the resonant value of $\omega = 1.50$ a.u., whereas the pulse duration 30 fs and intensity $2.5 \times 10^{14}$ W/cm$^2$ are kept fixed. One can see, that each photoionization spectrum in Fig. 4 consists of two parts. The largest major part is related to the $He^+(1s^1)$ photoionization threshold, and the somewhat smaller minor one corresponds to the population of the $He^+(2p^1)$ final state. At the resonant carrier frequency (the middle spectrum), the two ionic states mix completely, and a typical dynamical Autler-Townes doublet [43] with approximately equal intensities can be seen. One can see that the computed spectra in Fig. 4 exhibit prominent multiple-peak pattern, which are due to the dynamic in-

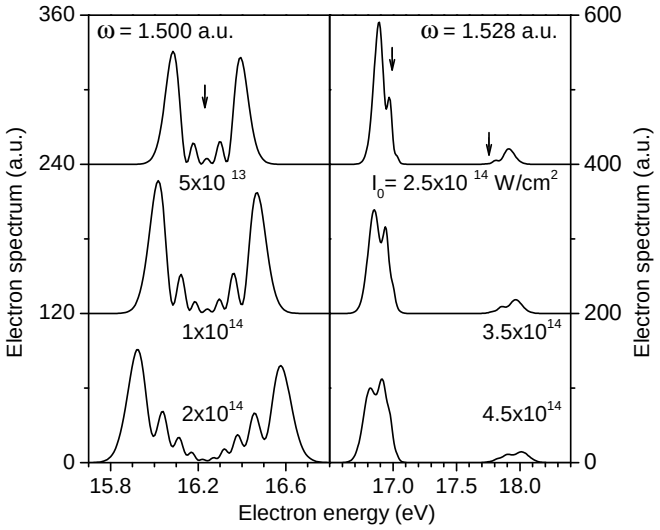


FIG. 5: Photoionization spectra of the helium atom computed for Gaussian-shaped pulses of 30 fs duration, two carrier frequencies of 1.500 a.u. (*left panel*) and 1.528 a.u. (*right panel*), and different peak intensities (indicated near each spectrum). For further details, see caption of Fig. 4. The complexity of the dynamic interference patterns in the spectrum increases with the increase of the pulse intensity.

terference [39, 40, 42, 43]. The number of interference peaks increases with the energy shift of the ionization threshold, which is larger for smaller energy detunings.

The two uppermost spectra represent the photon energies below the resonant value of $\omega = 1.50$ a.u. In this case, the dressed $\mathrm{He}^+(1s^1)$ ionic state is just below the $\mathrm{He}^+(2p^1)$ one: $E(1s_{ion}) + \omega < E(2p_{ion})$. The former experiences a negative energy shift and the latter a positive one. Therefore, photoelectrons corresponding to the $\mathrm{He}^+(1s^1)$ threshold acquire a positive shift, and the major part of the spectrum shifts to the high-energy side from the central photoelectron energy $\varepsilon_0 = \omega - IP$ (indicted by the vertical down-arrow in the figure). On the contrary, the minor part of the spectrum, which corresponds to the $\mathrm{He}^+(2p^1)$ threshold, experiences the negative energy shift. The situation is altered for the photon energies above the resonant value (two lowermost spectra in Fig. 4). The dressed $\mathrm{He}^+(1s^1)$ state is now above the $\mathrm{He}^+(2p^1)$ ionic state: $E(1s_{ion}) + \omega > E(2p_{ion})$. As a result, the former experiences a positive energy shift and the latter a negative one. The corresponding major part of the spectrum shifts now to the low-energy side from the central photon energy $\varepsilon_0$, and the minor part accordingly to the high-energy side.

Figure 5 demonstrates changes of the dynamic interference in the photoionization spectra computed for different pulse intensities. For the resonant carrier frequency (left panel), a typical Autler-Townes doublet structured by interference patterns [42, 43] can be observed. As usual, the number of interference peaks increases with the growth of the pulse intensity (from top to bottom of the figure). The same observation applies to the off-resonant regime (right panel, carrier frequency is larger than its resonant value). The energy shift in the spectrum from the central electron energy $\varepsilon_0$ (indicated by the vertical down-arrow) grows as a function of the pulse intensity. As a consequence, the number of peaks in the spectrum grows as well. The interference structure computed for the largest considered intensity of $4.5 \times 10^{14}$ W/cm$^2$ (the lowermost right spectrum in Fig. 5 ), is somewhat truncated on the low-energy side. This behavior indicates that the photoionization process is nearly-saturated at this relatively large peak intensity.

### B. Explicit estimates of the electron spectrum

So far we discussed results of the numerical calculations of the two-electron wave packet propagation dynamics in He. Such an accurate theoretical description of the process is very time-consuming. Therefore, it is very important to wield a simple theoretical model which can provide quick and reliable estimates for the dynamic interference effects in the photoelectron spectrum of He. It has been introduced in the supplemental material document of our previous work [39]. Below we briefly outline this model and apply it to estimate selected numerical spectra. For transparency, we explicitly assume that only two subsequent ionization steps of an atom are possible (as in He), and only one final ionic state is presented in each of the photoionization steps. Generalization of the theory to the case of several ionization thresholds in each step is straightforward.

We now restrict the ansatz for the total wave function of the system $\Psi(t)$ to the quantum motion of only essential electronic states participating directly in the photoionization dynamics in each step. It thus includes: (i) the neutral ground electronic state $|N\rangle$ of energy of $E_N = 0$ (chosen as the origin of the energy scale); (ii) the electron continuum states of the singly-ionized atom $|F\varepsilon\rangle$ of energy $IP + \varepsilon$ (where $IP = E_F - E_N$ stays for the ionization potential to produce state $|F\rangle$ and $\varepsilon$ is the kinetic energy of the primary photoelectron); and (iii) the final doubly-ionized electron continuum states $|G\varepsilon\varepsilon'\rangle$ of energy $DIP + \varepsilon + \varepsilon'$ (where $DIP = E_G - E_N$ is the double-ionization potential to produce state $|G\rangle$ and $\varepsilon'$ is the kinetic energy of the secondary electron emitted by the ionization of the ion). Following Refs. [39–43], the total wave function of the system reads

$$\Psi(t) = a_N(t)|N\rangle + \int d\varepsilon\, a_\varepsilon(t)|F\varepsilon\rangle e^{-i\omega t} + \iint d\varepsilon d\varepsilon'\, b_{\varepsilon\varepsilon'}(t)|G\varepsilon\varepsilon'\rangle e^{-2i\omega t}. \quad (20)$$

In Eq. (20), $a_N(t)$, $a_\varepsilon(t)$, and $b_{\varepsilon\varepsilon'}(t)$ are the time-dependent amplitudes for the population of the initial neutral state, the singly- and the doubly-ionized continuum states, respectively. The continuum states are already dressed by the energy of photons absorbed in order

to access these states. Technically, the stationary states have just been redefined by multiplying with the phase factors $e^{i\omega t}$ and $e^{2i\omega t}$ [41]. Inserting $\Psi(t)$ into the time-dependent Schrödinger equation for the total Hamiltonian of the atom plus its interaction with the laser field, and implying the rotating wave [70] and local [71, 72] approximations, we obtain the following set of equations for the amplitudes [39–43]

$$i\dot{a}_N(t) = \left(\Delta_N - \tfrac{i}{2}\Gamma_N\right) g^2(t)\, a_N(t), \tag{21a}$$

$$i\dot{a}_\varepsilon(t) = \left\{\tfrac{1}{2} d_\varepsilon \mathcal{E}_0\right\} g(t)\, a_N(t) + \left(IP + \left[\Delta_I - \tfrac{i}{2}\Gamma_I\right] g^2(t) + \varepsilon - \omega\right) a_\varepsilon(t), \tag{21b}$$

$$i\dot{b}_{\varepsilon\varepsilon'}(t) = \left\{\tfrac{1}{2}\widetilde{d}_{\varepsilon'} \mathcal{E}_0\right\} g(t)\, a_\varepsilon(t) + (DIP + \varepsilon + \varepsilon' - 2\omega)\, b_{\varepsilon\varepsilon'}(t). \tag{21c}$$

Here, $d_\varepsilon = \langle F\varepsilon|\hat{z}|N\rangle$ and $\widetilde{d}_{\varepsilon'} = \langle G\varepsilon'|\hat{z}|F\rangle$ are the energy-dependent dipole transition matrix elements for the ionizations of the neutral atom and of the ion, respectively.

One can see that the populations of the neutral ground and the singly-ionized states are subjects to the time-dependent leakages, $-\frac{i}{2}\Gamma_N g^2(t)$ and $-\frac{i}{2}\Gamma_I g^2(t)$, which is due to photoionization of these states by strong high-frequency pulse. In addition, the energy of the neutral ground state is augmented by the time-dependent ac Stark shift $\Delta_N\, g^2(t)$ [39, 40]. Similar shift $\Delta_I\, g^2(t)$ is introduced to the energy of the singly-ionized state. We stress, that even if the photon energy $\omega$ is insufficiently large to further ionize the ion (as in the present case), the shift $\Delta_I$ also exists, and it is caused by the coupling in the discrete spectrum of the singly-ionized system. However, leakage in the ion in this case is equal to zero, $\Gamma_I = 0$. Therefore, dynamics in the photoionization step can now be decoupled from the dynamics of the electron remaining bound to the ion. Neglecting also the ac Stark shift in continuum for the neutral ground state $\Delta_N \approx 0$, the final equations describing photoionization process read

$$i\dot{a}_N(t) = -\tfrac{i}{2}\Gamma_N\, g^2(t)\, a_N(t), \tag{22a}$$

$$i\dot{a}_\varepsilon(t) = \left\{\tfrac{1}{2} d_\varepsilon \mathcal{E}_0\right\} g(t)\, a_N(t) + \left(IP + \Delta_I\, g^2(t) + \varepsilon - \omega\right) a_\varepsilon(t). \tag{22b}$$

The above derived equations of motion (22) can be applied to compute the photoelectron spectrum, $\sigma(\varepsilon) = |a_\varepsilon(\infty)|^2$. The two parameters $\Delta_I$ and $\Gamma_N$ needed can be estimated from first principles or taken to be fit parameters. We follow here the former path. For simplicity, we restrict further consideration to the major part of the photoionization spectrum, which corresponds to the $He^+(1s^1)$ ionization threshold. The direct ionization rate $\Gamma_N$ can be computed with the help of the total photoionization cross section of the neutral ground state of He via $\Gamma_N = 2\pi|\frac{1}{2} d_\varepsilon \mathcal{E}_0|^2 = \sigma_\varepsilon I_0/\omega$ [25, 41]. For the present purpose, it was sufficient to estimate the corresponding dipole transition amplitude $d_\varepsilon$ and the total cross section $\sigma_\varepsilon$ at the Hartree-Fock level. The shift $\Delta_I$ in the $He^+$ ion was computed through the diagonalization of the matrix (18), which describes the quantum motion of the dressed $1s_{ion}$ state coupled by the field to the motion of the whole $np_{ion}$ electron spectrum. It neglects, however, the quantum motion of states with different angular momenta $ns_{ion}$, $nd_{ion}$, etc. Since the photon energy $\omega$ is nearly-resonant to the $1s_{ion} \to 2p_{ion}$ transition, it provides the main contribution to the shift. Eq. (18) thus yields a reliable estimate for $\Delta_I$.

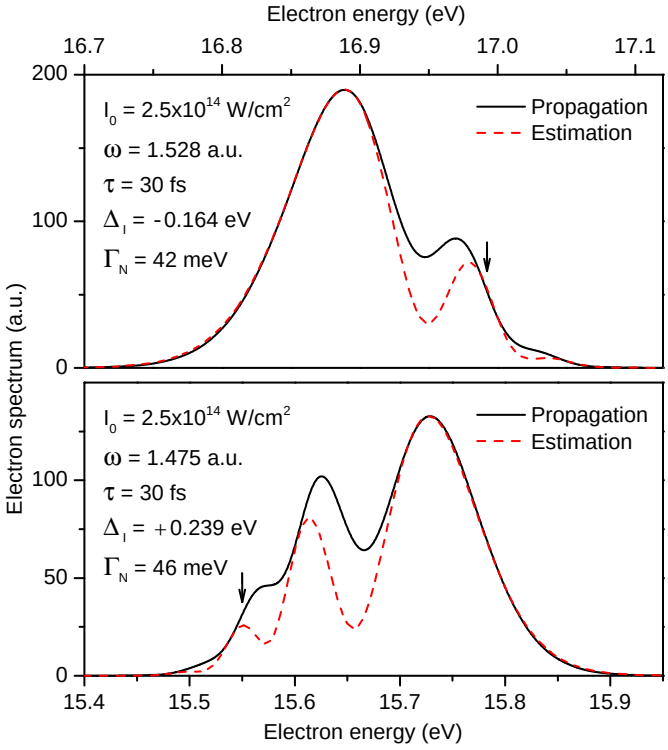


FIG. 6: (Color online) Comparison of the dynamic interference patterns in the major part of the photoionization spectrum, which corresponds to the $He^+(1s^1)$ final state, computed numerically via the electron wave packet propagation and estimated as described in Sec. III B for two Gaussian-shaped pulses. The computational parameters are indicated in the panels. Each estimated spectrum is normalized to the maximum of the corresponding numerical one.

Results of the present estimation of the two selected numerical spectra are collected in Fig. 6. The pulse properties and parameters $\Delta_I$ and $\Gamma_N$ used in the propagation and for the estimation of the spectra are indicated in each panel. One can see that Eq. (22) provides an overall good estimate for the major part of the numerical spectra related with the $He^+(1s^1)$ ionization threshold. Each pair of the estimated and computed spectra possesses an equal number of oscillations caused by the dynamic interference. The energy positions and relative heights of the multiple peak structures are however slightly differ-

ent. The dynamic interference is very sensitive to the time-dependence and to the absolute values of the energy shifts $\Delta_I$ and ionization rates $\Gamma_N$ [39, 40, 42, 43]. In Eq. (22), the energy shift $\Delta_I$ explicitly follow the pulse intensity envelope $I_0 g^2(t)$, which is typical for the ac Stark effect [7]. For the resonant carrier frequencies, the energy splitting between the dynamical Autler-Townes doublet follows the time-envelope of the field $\mathcal{E}_0 g(t)$ [42, 43]. The present situation is intermediate to those two extremes, which can be one of the reasons for a slight disagreement between the estimated and computed spectra in Fig. 6. Improvement can probably be achieved by either a better calculation of or by fitting the parameters $\Delta_I$ and $\Gamma_N$. Fig. 6 demonstrates that a simplified and explicit description of the process is possible via Eq. (22) which leads to a better understanding of the findings and can be used for a quick but rather reliable estimate of the dynamic interference in He.

## IV. CONCLUSION

The time-dependent Schrödinger equation for the helium atom exposed to coherent intense high-frequency short linearly-polarized laser pulse is solved by numerically propagating the two-active-electron wave packet. The propagation over very large spatial grids and long times, required to allow for the interference of electron wave packets emitted at different times to take place, is managed by the efficient time-dependent restricted-active-space configuration-interaction method. Working equations for the application of the TD-RASCI method to the photoionization of He are collected and discussed.

The carrier frequencies of the pulse were chosen to be nearly-resonant for the $He^+(1s \to 2p)$ transition, which is sufficient to ionize neutral He by one-photon absorption, but not enough to further ionize the ion by absorption of a subsequent photon from the pulse. We allowed only one of the electrons in He to be ionized during the propagation, whereas the other electron feels the field and is active but was kept bound to the nucleus. The present active space was restricted to the electron configurations which describe: (i) one-electron photoionization and above threshold ionization of He; (ii) relaxation of the remaining $1s$ electron in response to the photoionization; and (iii) excitation of this bound electron explicitly in the $2p$ state and in an effective way in the whole $np$ electron spectrum. As a result, the present calculations account for sequential two-photon absorption, as well as for main but all three-photon absorption processes in a numerically precise way.

The presently computed electron energy spectra exhibit two photoionization structures, which are due to the population of the $He^+(1s^1)$ and $He^+(2p^1)$ final ionic states by one- and, respectively, two-photon absorption. The above-threshold ionization peaks, related to those thresholds and produced respectively by two and three-photon absorption processes, are also visible. The photoionization peaks exhibit distinct patterns which are due to dynamic interference. The effect is exclusively produced by the dynamics of the electron remaining in $He^+$, which is governed by the nearly-resonant intense coherent laser pulse and is coupled to the dynamics of the photoelectron. One can view this processes as if the $1s$ and $2p$ ionization thresholds, seen by the photoelectrons, experience the opposite time dependent energy shifts provided by the pulse. This results in the emission of photoelectrons with different kinetic energies along the pulse, which is at the heart of the dynamic interference phenomenon.

The dynamic interference pattern can be controlled by choosing carrier frequencies across the $He^+(1s \to 2p)$ resonant transition and different pulse intensities. The relative intensities of the two photoionization peaks, associated with the $He^+(1s^1)$ and $He^+(2p^1)$ ionization thresholds, depend on the photon energy detuning. For the resonant carrier frequency of 1.50 a.u., a nearly-symmetric interference-structured Autler-Townes doublet can be observed. Finally, we notice that the carrier frequencies, pulse durations, field intensities, and temporal coherence required to produce observable effects, are available at present at the FEL facility FERMI@Elettra [14]. Our results provide a theoretical background for future experimental verification of the dynamic interference effect in the high-frequency regime.

### Acknowledgments

This work was partly supported by the State Hessen Initiative for the Development of Scientific and Economic Excellence (LOEWE) within the focus-project Electron Dynamics of Chiral Systems (ELCH) and by the U.S. ARL and the U.S. ARO under Grant No. W911NF-14-1-0383. Ph.V.D. acknowledges Research Institute of Physics, Southern Federal University for support within the inner project no. 213.01.-07.2014/11PPIG and for the hospitality during his research stay there.

[1] K. Rzążewski, Phys. Rev. A **28**, 2565 (1983).
[2] K. Rzążewski, J. Zakrzewski, M. Lewenstein, and J. W. Haus, Phys. Rev. A **31**, 2995 (1985).
[3] M. Lewenstein, J. Zakrzewski, and K. Rzążewski, J. Opt. Soc. Am. B **3**, 22 (1986).
[4] E.J. Robinson, J. Phys. B **19**, L657 (1986).
[5] D. Rogus and M. Lewenstein, J. Phys. B **19**, 3051 (1986).
[6] J.N. Bardsley, A. Szöke and M.J. Comella, J. Phys. B **21**, 3899 (1988).
[7] B.J. Sussman, Am. J. Phys. **79**, 477 (2011).
[8] R.R. Jones, Phys. Rev. Lett. **74**, 1091 (1995).
[9] R.R. Jones, Phys. Rev. Lett. **75**, 1491 (1995).

[10] F. Krausz and M. Ivanov, Rev. Mod. Phys. **81**, 163 (2009).
[11] G. Sansone, E. Benedetti, F. Calegari, *et al.*, Science **314**, 443 (2006).
[12] E. Goulielmakis, M. Schultze, M. Hofstetter, *et. al.*, Science **320**, 1614 (2008).
[13] W. Ackermann, G. Asova, V. Ayvazyan, *et al.*, Nature photonics **1**, 336 (2007).
[14] Home page of FERMI at Elettra in Trieste, Italy, www.elettra.trieste.it/lightsources/fermi/machine.html
[15] L. Young, *et al.,* Nature **466**, 56 (2010).
[16] B. Rudek, *et al.,* Nature Photonics **6**, 858 (2012).
[17] B. Rudek, *et al.,* Phys. Rev. A **87**, 023413 (2013).
[18] K. Motomura, *et al.,* J. Phys. B: At. Mol. Opt. Phys. **46**, 164024 (2013).
[19] L.A.A. Nikolopoulos, T.J. Kelly and J.T. Costello, Phys. Rev. A **84**, 063419 (2011).
[20] N. Rohringer and R. Santra, Phys. Rev. A **77**, 053404 (2008).
[21] E.P. Kanter, *et al.,* Phys. Rev. Lett. **107**, 233001 (2011).
[22] N. Rohringer and R. Santra, Phys. Rev. A **86**, 043434 (2012).
[23] S. Pabst, D. Wang, and R. Santra, Phys. Rev. A **92**, 053424 (2015).
[24] J.-C. Liu, Y.-P. Sun, C.-K. Wang, H. Ågren, and F. Gel'mukhanov, Phys. Rev. A **81**, 043412 (2010).
[25] Y.-P. Sun, J.-C. Liu, C.-K. Wang, and F. Gel'mukhanov, Phys. Rev. A **81**, 013812 (2010).
[26] Ph.V. Demekhin, S.D. Stoychev, A.I. Kuleff and L.S. Cederbaum, Phys. Rev. Lett. **107**, 273002 (2011).
[27] Ph.V. Demekhin, K. Gokhberg, G. Jabbari, S. Kopelke, A.I. Kuleff, and L.S. Cederbaum, J. Phys. B: At. Mol. Opt. Phys. **46**, 021001 (2013).
[28] Ph.V. Demekhin and L.S. Cederbaum, Phys. Rev. A **91**, 013417 (2015).
[29] C. Buth, *et al.,* J Chem. Phys. **136**, 214310 (2012).
[30] S.M. Cavaletto, C. Buth, Z. Harman, E.P. Kanter, S.H. Southwort, L. Young and C.H. Keitel, Phys. Rev. A **86**, 033402 (2012).
[31] C. Weninger and N. Rohringer, Phys. Rev. A **88**, 053421 (2013).
[32] V. Kimberg and N. Rohringer, Phys. Rev. Lett. **110**, 043901 (2013).
[33] C Weninger, *et al.,* Phys. Rev. Lett. **111**, 233902 (2013).
[34] L.S. Cederbaum, Y.-C. Chiang, Ph.V. Demekhin, and N. Moiseyev, Phys. Rev. Lett. **106**, 123001 (2011).
[35] Ph.V. Demekhin, Y.-C. Chiang, and L.S. Cederbaum, Phys. Rev. A **84**, 033417 (2011).
[36] Ph.V. Demekhin and L.S. Cederbaum, J. Phys. B: At. Mol. Opt. Phys. **46**, 164008 (2013).
[37] K. Toyota, O.I. Tolstikhin, T. Morishita, S. Watanabe, Phys. Rev. A **76**, 043418 (2007).
[38] K. Toyota, O.I. Tolstikhin, T. Morishita, S. Watanabe, Phys. Rev. A **78**, 033432 (2008).
[39] Ph.V. Demekhin and L.S. Cederbaum, Phys. Rev. Lett. **108**, 253001 (2012).
[40] Ph.V. Demekhin and L.S. Cederbaum, Phys. Rev. A **88**, 043414 (2013).
[41] Ph.V. Demekhin and L.S. Cederbaum, Phys. Rev. A **83**, 023422 (2011).
[42] A.D. Müller and Ph.V. Demekhin, J. Phys. B: At. Mol. Opt. Phys. **48**, 075602 (2015).
[43] Ph.V. Demekhin and L.S. Cederbaum, Phys. Rev. A **86**, 063412 (2012).
[44] *NIST Atomic Spectra Database* (National Institute of Standards and Technology, Gaithersburg, MD, 2012), http://physics.nist.gov/PhysRefData/ASD/index.html
[45] S.H. Autler and C.H. Townes, Phys. Rev. **100**, 703 (1955).
[46] J. Zanghellini, M. Kitzler, C. Fabian, T. Brabec, and A. Scrinzi, Laser Phys. **13**, 1064 (2003).
[47] T. Kato and H. Kono, Chem. Phys. Lett. **392**, 533 (2004).
[48] M. Nest, T. Klamroth, and P. Saalfrank, J. Chem. Phys. **122**, 24102 (2005).
[49] O.E. Alon, A.I. Streltsov and L.S. Cederbaum, J. Chem. Phys. **127**, 154103 (2007).
[50] D.J. Haxton, K.V. Lawler, and C. W. McCurdy, Phys. Rev. A **83**, 063416 (2011).
[51] D. Hochstuhl and M. Bonitz, J. Chem. Phys. **134**, 084106 (2011).
[52] D. Hochstuhl and M. Bonitz, Phys. Rev. A **86**, 053424 (2012).
[53] F. Robicheaux, J. Phys. B **45**, 135007 (2012).
[54] J. Colgan and M.S. Pindzola, Phys. Rev. Lett. **108**, 053001 (2012).
[55] J. Colgan, A. Emmanouilidou, and M.S. Pindzola, Phys. Rev. Lett. **110**, 063001 (2013).
[56] M.S. Pindzola, C.P. Ballance, Sh.A. Abdel-Naby, F. Robicheaux, G.S.J. Armstrong, and J. Colgan, J. Phys. B **46**, 035201 (2013).
[57] S. Bauch, L.K. Sørensen, and L.B. Madsen, Phys. Rev. A **90**, 062508 (2014).
[58] S. Chattopadhyay, S. Bauch, and L.B. Madsen, Phys. Rev. A **92**, 063423 (2015).
[59] Ph.V. Demekhin, D. Hochstuhl, and L.S. Cederbaum, Phys. Rev. A **88**, 023422 (2013).
[60] A.N. Artemyev, A.D. Müller, D. Hochstuhl, and Ph.V. Demekhin, J. Chem. Phys. **142**, 244105 (2015).
[61] D.E. Manolopoulos and R.E. Wyatt, Chem. Phys. Lett. **152**, 23 (1988).
[62] T.N. Rescigno and C.W. McCurdy, Phys. Rev. A **62**, 032706 (2000).
[63] C.W. McCurdy, M. Baertschy and T.N. Rescigno, J. Phys. B: At. Mol. Opt. Phys. **37**, R137 (2004).
[64] D.A. Varshalovich, A.N. Moskalev, and V.K. Khersonskii, *Quantum Theory of Angular Momentum* (World Scientific Pub., Singapore 1988).
[65] J.A. Gaunt, Phil. Trans. R. Soc. Lond. A **228**, 151 (1929).
[66] T.J. Park and J.C. Light, J. Chem. Phys. **85**, 5870 (1986).
[67] S.L. Carter and H.P. Kelly, Phys. Rev. A **16**, 1525 (1977).
[68] V.L. Sukhorukov, B.M. Lagutin, I.D. Petrov, H. Schmoranzer, A. Ehresmann, and K.H. Schartner, J. Phys. B **27**, 241 (1994).
[69] Ph.V. Demekhin, B.M. Lagutin and I.D. Petrov, Phys. Rev. A **85**, 023416 (2012).
[70] D.J. Griffiths, *Introduction to Quantum Mechanics* (Prentice-Hall, New Jersey, 1994).
[71] L.S. Cederbaum and W. Domcke, J. Phys. B. **14**, 4665 (1981).
[72] W. Domcke, Phys. Rep. **208**, 97 (1991).